HUBC Excellence Project
Annual Report
David Whiteman, Zhifeng Yang, Xingchao Chen

Project Research Progress Summary of Main Accomplishments

- Data from 11 radars processed to create super-observation dataset for assimilation
- Successfully assimilated 11 radar super-observation data into the WRF model
- Collected data from four lidar systems for the July 14 case from the PECAN campaign
- Currently debugging ALVICE lidar data assimilation code

1. Introduction

An undular bore is a wave disturbance, which can happen both in the atmosphere and in the water. In the atmosphere, the undular bore can be recognized through the smooth bands of clouds that form in the lower atmosphere. This phenomenon can be found in various locations. The best known of these events are called "morning glory" bores, which are bands of clouds along the coast of Australia's Gulf of Carpentaria. In water, the undular bore consists of the waves generated by dropping a pebble into a pond. Here we address the following questions: What causes an undular bore? What kind of weather will be affected after the occurrence of the undular bore?

An undular bore in the atmosphere is generated when a cold front collides with a stable air mass in the warm and moist sector pf the atmosphere (Figure 1a). As the cold front intrudes on the less stable warm sector, the warm layer is lifted up. Apart from the uplifting force, the lifted warm stable layer experiences a restoring force which causes parcels to oscillate around an equilibrium position. While the air is lifted up, the temperature decreases and, if the temperature reaches the condensation point, clouds can form. Therefore, clouds will only form along the wave crests thus generating bands of clouds. Figure 1a shows the process of the collision of a cold front with a warm stable layer. Because of the collision, the surface will become colder than the upper layer air, which forms the more stable inversion layer (Figure 1b).

However, the cold front will move with a proper speed depending on the prevailing weather conditions. If the cold front moves too slowly into the warm sector, the lifting will be weaker, and the undular waves may not develop. If the cold front moves quickly, the lifting will be stronger, and the waves may break apart.
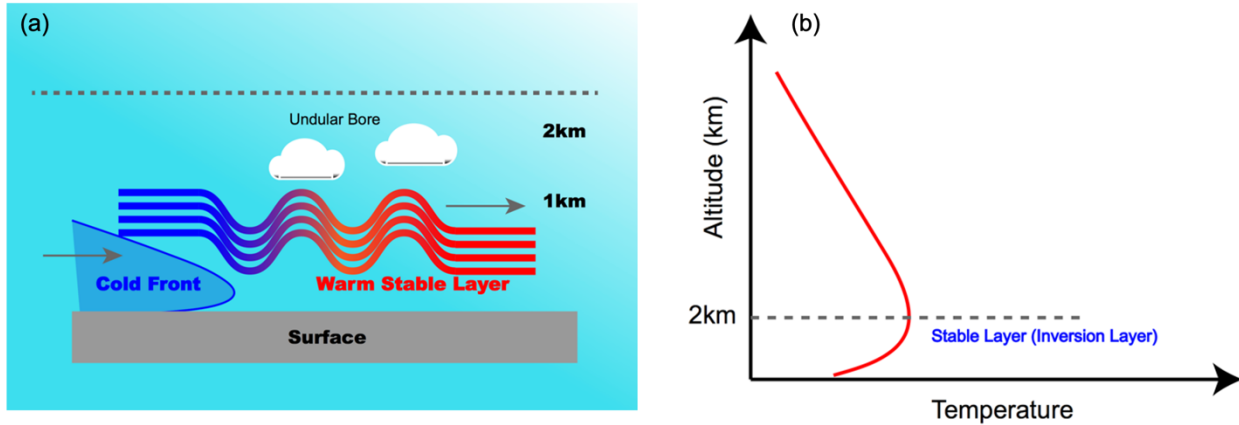
Figure 1. (a) Schematic representation of the collision between a cold front and a warm stable layer in the atmosphere. (b) Atmospheric temperature vertical profile.

Undular bore creation is related to the effects of severe weather, such as the outflow from a mesoscale convective complex, so that the propagating bore can initiate new thunderstorms ahead of the MCS.

Motivations and Novelty

The PECAN field campaign occurred during June – August, 2015 in the mid-west. It focused on improving the understanding and simulation of the processes that initiate and maintain convection and convective precipitation at night over the central portion of the Great Plains region of the United States. The motivation of this work is to improve the understanding and forecasting skill of nocturnal convection initiation by assimilating multiple Doppler weather radars and ground-based remote sensing water vapor profilers.

The novelty of this study is employing lidar water vapor assimilation (Raman, DIAL and airborne) and coupling Radar and lidar assimilation. The objective is to better understand the strength and limitations of each observation type, by assimilating radar and lidar separately and jointly.

2. Data Sets and Model Configuration
2.1 NEXRAD Radar

Weather Surveillance Doppler Radar (S-band Doppler weather radar) can detect precipitation and wind, and its data can be processed to map precipitation patterns and movement.
The radars scan 14 elevations every 5 mins (~ 3 elevations per min or one radar image per 20 sec). Detection ranges vary depending on different objects, e.g., 150 km (precipitation), 260 km (intense rain or snow), not detectable (light rain, light snow, or drizzle from shallow cloud weather systems). The radar sites used in this study are shown as red dots in Figure 2. More detailed information about the radar data can be found in Table 1.
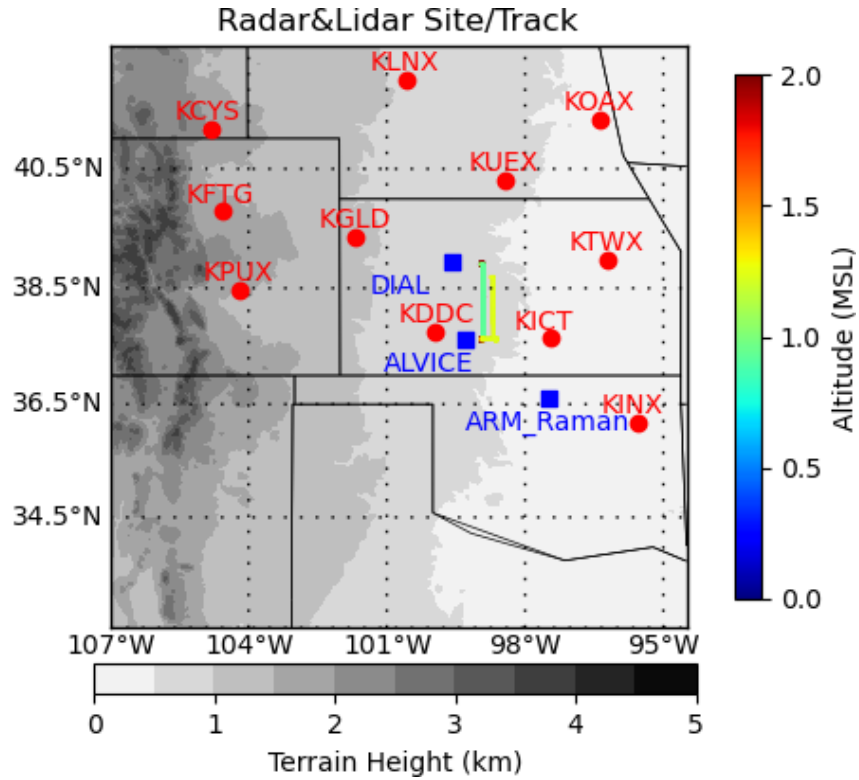
Figure 2. Terrain height in the study domain (white-black contour), overlaid with the radar sites (red dots with site names), lidar sites (blue squares with lidar names), and University of Wyoming King Air flight paths (color-coded line shows the flight path height).

Table 1. Radar site geolocation information and data availability on July 14, 2015.

Site	City	State	Latitude	Longitude	Altitude (m)	Data availability (UTC)
KCYS	Cheyenne	WY	41.15	-104.81	1887.0	0000-1000
KDDC	Dodge City	KS	37.76	-99.97	813.0	0000-1000
KEAX	Pleasant Hill	MO	38.81	-94.26	332.0	0000-0900
KGLD	Goodland	KS	39.37	-101.70	1132.0	0000-0600
KICT	Wichita	KS	37.65	-97.44	426.0	0000-0800
KINX	Inola	OK	36.18	-95.56	228.0	0000-1300
KLNX	North Platte	NE	41.96	-100.58	948.0	0000-1600
KOAX	Valley	NE	41.32	-96.37	384.0	0000-0900
KPUX	Pueblo	CO	38.46	-104.18	1634.0	0000-0800
KTWX	Topeka	KS	38.99	-96.23	431.0	0000-0800
KUEX	Blue Hill	NE	40.32	-98.44	626.0	0000-1100

2.2 Lidar data

This study employs water vapor vertical profile measurements from four lidars, i.e., ALVICE lidar, NCAR DIAL lidar, University of Wyoming King Air Compact Raman Lidar (CRL) lidar, and ARM Raman lidar. Figure 2 shows the lidar locations in blue squares. The flight paths of the University of Wyoming King Air are also indicated as color lines in Figure 2.

2.3 Study Domain and Model Configuration

The model domain covers Nebraska, Kansas, Colorado, Oklahoma, and north Texas (Figure 2). The Rocky Mountains are on the western edge of the study domain, with terrain height around 3 km. While the eastern part of the study domain over the state boundaries of Nebraska, Iowa, Kansas, and Oklahoma is generally flat, with terrain height below 0.5 km (Figure 2). The horizontal grid spacing is 3 km. The model domain uses the following number of grids: 401 (west-east) $\times$ 401 (south-north) $\times$ 61 (bottom-top). The highest model level is located at 50 hPa, and 19 vertical levels in the lowest 1 km above ground level (AGL) is designed to resolve the planetary boundary layer.

Model physics parameterizations

Physical parameterization schemes applied in the model include the six-species double-moment Thompson et al. (2008) microphysics scheme, unified Noah land surface model (Ek et al. 2003), Monin–Obukhov–Janjic′ Eta scheme (Janjic′ 1996) for surface layer parameterization, Mellor–Yamada–Janjic′ TKE scheme (Janjic′ 1994) for PBL processes, and the Rapid Radiative Transfer Model for General Circulation Models (RRTMG) schemes (Iacono et al. 2008) for longwave and shortwave radiation. Simulated radar reflectivity is calculated using the built-in module of the Thompson et al. (2008) microphysics scheme.

3. Experiment Design

3.1 Ensemble member generation

The NOAA Global Ensemble Forecast System (GEFS) has only 21 members but we wish to use 40 ensemble members for our work. The first GEFS ensemble member is the control member, the remaining 20 members are perturbed members. To generate the 40 ensemble members that we desire at 18Z July 13, 2015, the first 20 members are generated directly from ensemble members at 18Z July 13, 2015. The other 20 members are generated from the 6-hour forecast at 12Z July 13, 2015, which will be 18Z July 13, 2015.
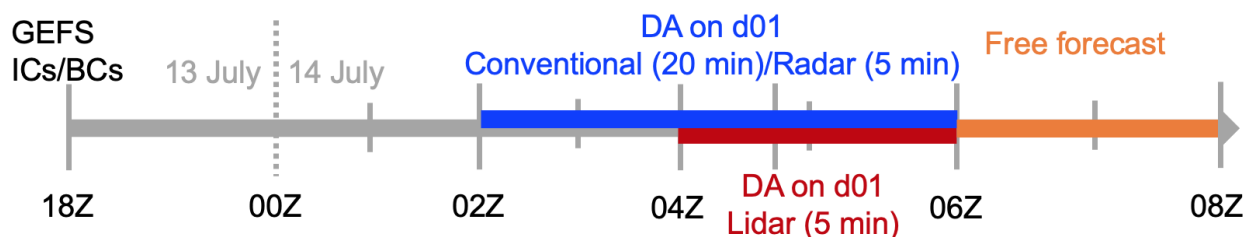
Figure 3. Timeline of model spin-up, the data assimilation cycling, and ensemble free forecasts. Based on initial and lateral boundary conditions from GEFS, a 40-member ensemble forecast is run between 1800Z July 13, 2015 and 0200 July 14, 2015 to provide the ensemble background for the first data assimilation cycle on the 3-km domain.

The ensemble WRF model was initiated using the initial and boundary conditions (ICs/BCs) from Global Ensemble Forecast System (GEFS) at 18Z July 13, 2015, to spin-up and stabilize the model (Figure 3). The first eight-hour model simulations are treated as spin-up and discarded (until 02Z July 14, 2015). The conventional surface data assimilation is from 02Z to 06Z, and its assimilation window is 20 min (equal to report interval of METAR stations). Other assimilated observations are created as follows. The radar data assimilation starts at 02Z and lasts until 06Z. The assimilation window is 5 min. The assimilated variables include radial velocity and reflectivity. The lidar assimilation starts from 04Z to 06Z. The free forecast is from 06Z to 08Z, which is used to evaluate the radar and lidar data assimilation performance.

The designed experiments are shown in Table 2. The baseline experiment is to test the performance only assimilating conventional meteorological observations (e.g., radiosonde, surface, etc). The RAD experiment is to verify the performance of assimilating both conventional meteorological observations and radar reflectivity and radial velocity. The LID experiment is to check the assimilation of lidar water vapor mixing ratio observations. Finally, the RADLID experiment is to examine the performance of assimilating all the observation data.

Table 2. Designed experiments

Experiment	DA (Y or N)		Purpose
	Domain 01 (d01, 3 km)	Domain 02 (d02, 1 km)	
Spin-up: 18Z 13 July	Domain 01 (d01, 3 km)	Domain 02 (d02, 1 km)	Purpose d01: mesoscale meteorology; d02: bore wave
Baseline	Y/N	N/N	Performance only with Conventional DA i) temperature ii) wind iii) pressure
RAD	Y/Y(R*)	N/N	Performance with Conventional and Radar DA i) reflectivity ii) radial velocity
LID	Y/Y(L**)	N/N	Performance with Conventional and Lidar DA i) water vapor mixing ratio
RADLID	Y/Y(RL)	N/N	Performance with both Conventional, Radar & Lidar DA

*: Radar, **: Lidar
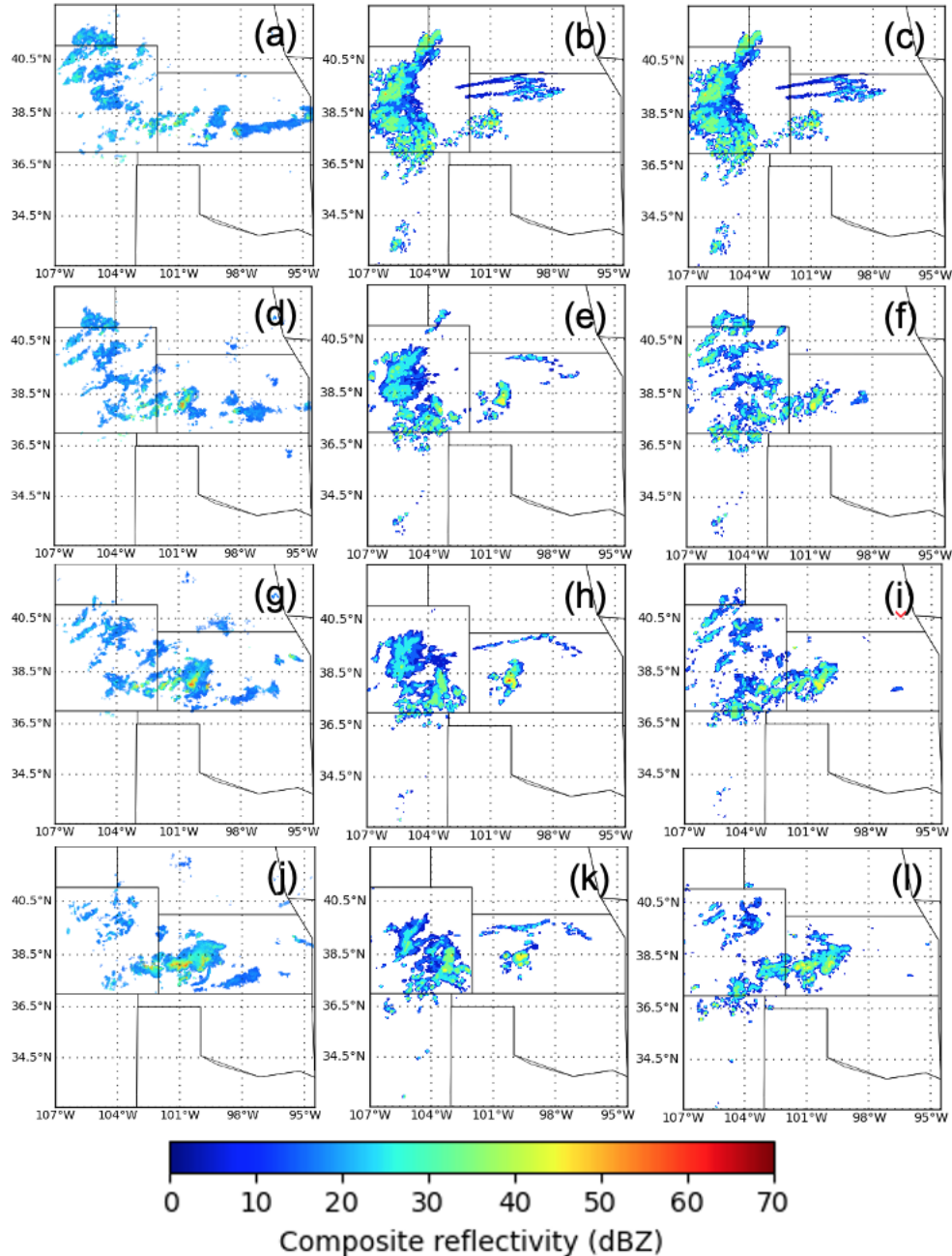
Preliminary results

Figure 4. Composite reflectivity from NEXRAD radar (first column), ensemble model simulation (second column), and radar assimilation (third column). Except that the first row does not include assimilation. The first to fourth rows are at 0200Z (a, b, c), 0300Z (d, e, f), 0400Z (g, h, i), and 0500Z (j, k, l) July 14, 2015, respectively.

Before assimilating radar data, the ensemble model simulation shows spurious clouds over Colorado (Figure 4b, c), which is significantly different from the radar observed composite reflectivity (Figure 4a). At 0300Z July 14, 2015, after 1-hour assimilation of radar reflectivity and radial velocity (12 assimilation cycles), the model simulated composite reflectivity appears similar to radar observation (Figure 4d, f). It means EnKF is successfully assimilating radar data into the WRF model. The ensemble model simulation still has strong spurious clouds over

Colorado. However, the model assimilation missed the clouds over eastern Kansas. The possible reason is that all the ensemble members did not capture this short life-time system (0000-0400Z July 14, 2015). After three hours, the spurious clouds occurred in southern Colorado, primarily due to the fact that even the lowest radar scan at 0.58 elevation angle can be 1–2 km above the surface in regions 100–200 km away from the radar site and there are no radar observations available to remove the excessive amount of hydrometeors near the surface.
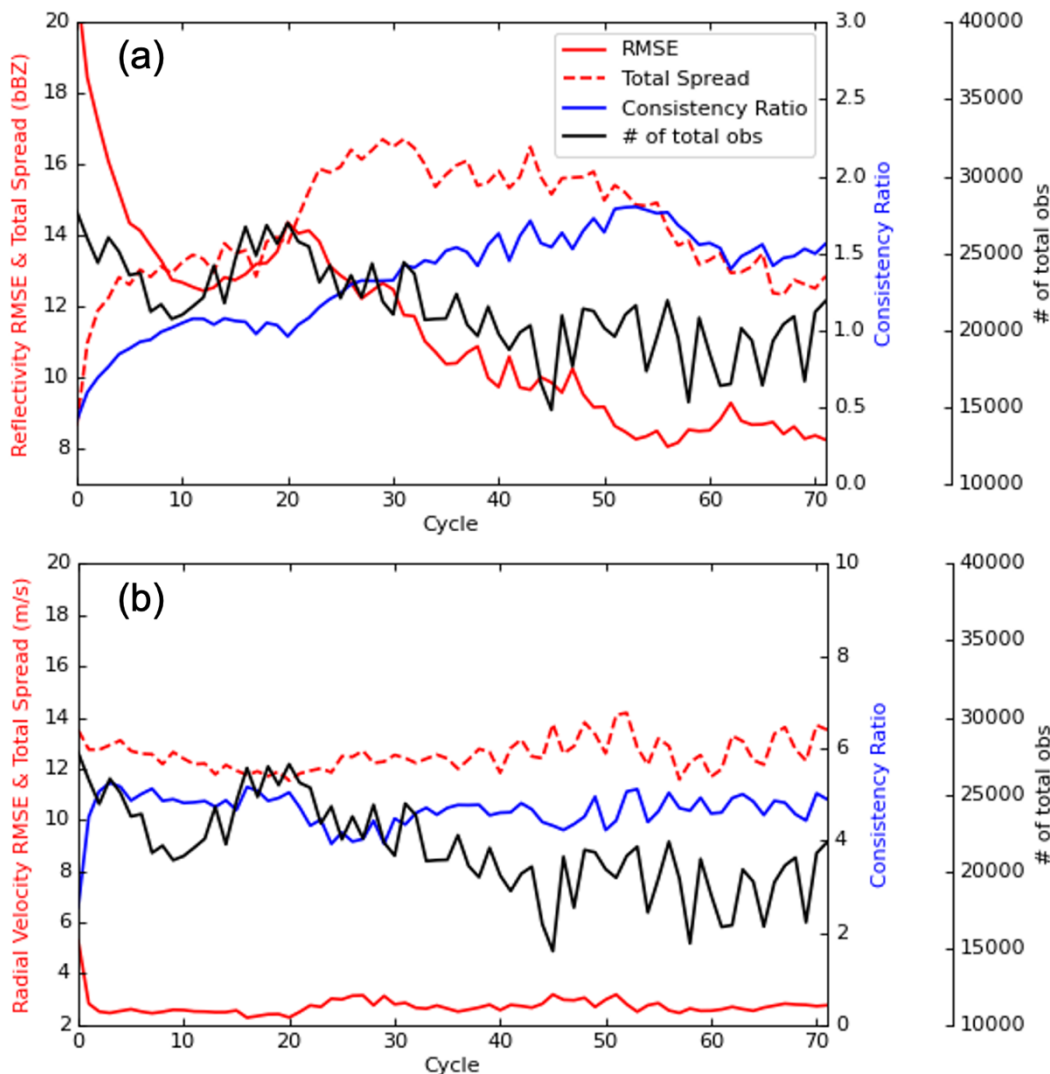

Figure 5. Evolution of RMSE (solid red line), total spread (dashed red line), consistency ratio (solid blue line), and the number of total radar observations (solid black line) for both reflectivity (a) and radial velocity (b).

The diagnostics of radar assimilation performance can be quantified by the following statistical metrics, e.g., Root Mean Square Error (RMSE), total spread (defined as the square root of both model spread and observation spread), consistency ratio (He et al, 2019). Figure 5 shows the evolution of these statistical metrics for both reflectivity and radial velocity, as well as the number of total radar observations. The reflectivity RMSE decreases consistently from 20 dBZ at

the first assimilation cycle to 8 dBZ at the last assimilation cycle (Figure 5a). It means the model simulation is approaching to the radar observed reflectivity. The total spread remains within 10 ~ 16 dBZ to insure that the ensemble members diverge from each other. Consequently, the consistency ratio remains within 1.0 ~ 1.5 through the whole assimilation period. Meanwhile, the number of total radar observations is approximately 20000, which is sufficient to perform the radar assimilation. For the radial velocity, the RMSE decreases sharply after the first few cycles, then remains stable around 3 m s^{-1}. The radial velocity total spread and consistency ratio remain stable as well (Figure 5b).
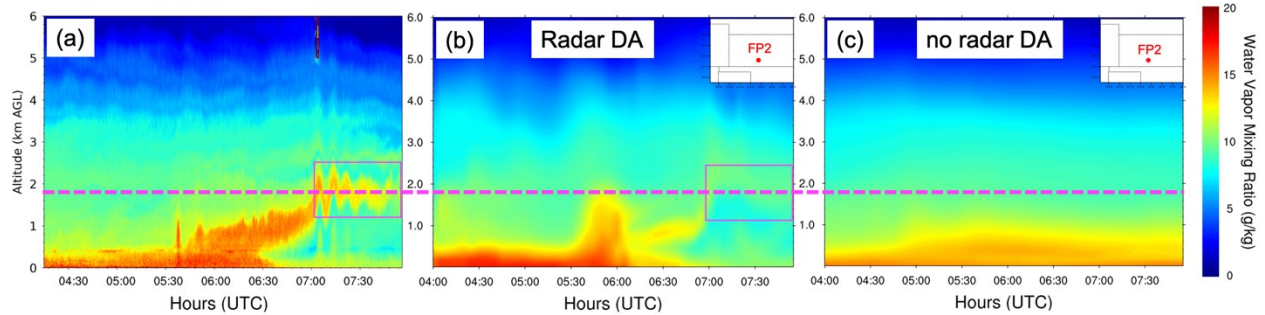

Figure 6. Water vapor mixing ratio vertical profile time series from ALVICE lidar observation (a), model with radar assimilation (b), and model without radar assimilation (c). The inset map on the upper right shows the location of FP2.

After assimilating radar data, the water vapor field is expected to be closer to the lidar observations. The ALVICE water vapor and model simulated water vapor vertical profiles from both with radar assimilation and without radar assimilation are presented in Figure 6. ALVICE observed water vapor was 20 g kg^{-1} below 1 km before being lifted up at 0630Z July 14, 2015. A bore wave occurred at 0700Z, resulting from gravity and lifting force. The equilibrium height is 1.8 km, and wave amplitude is about 0.5 km (Figure 6a). After assimilating radar data, a water vapor layer is lifted to ~ 2.0 km and an oscillating wave pattern can be observed in Figure 6b more similar to the actual lidar measuremnets. The water vapor vertical profile time series from model simulation without radar assimilated shows a relatively flat water vapor distribution below 1 km, with water vapor mixing ratio is around 13 g kg^{-1} (Figure 6c).
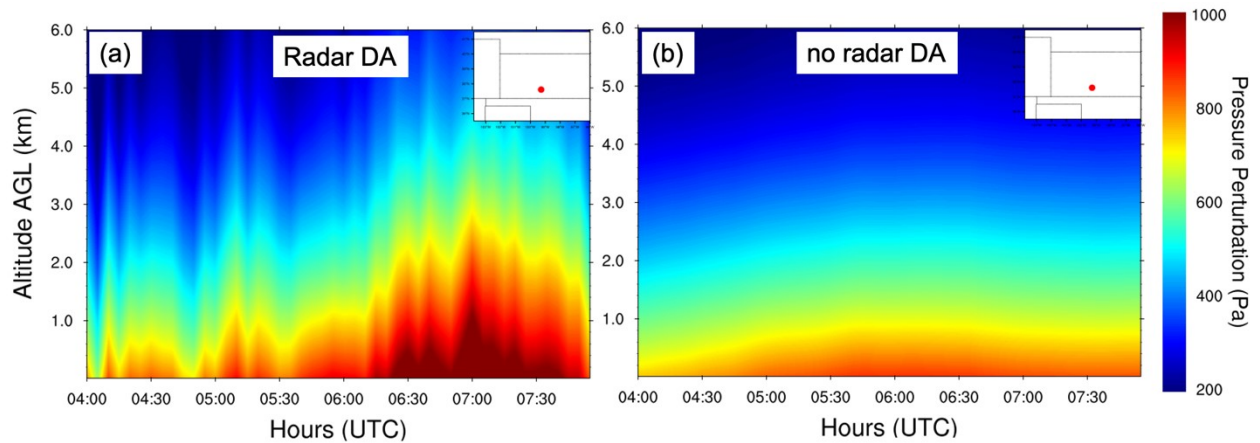
Figure 7. Pressure perturbation vertical profile time series from model with radar assimilation (a), and model without radar assimilation (b). The inset map on the upper right shows the location of FP2.

The wave propagation pattern is more obvious from the pressure perturbation vertical profile time series (Figure 7). The model simulated pressure perturbation vertical profile with radar data assimilated shows that bore wave pattern is significant, both before 0530Z and after 0615Z July 14, 2015 (Figure 7a). However, no wave pattern was found in the model simulated pressure perturbation vertical profile without radar data assimilated (Figure 7b).

Conclusions and Future Work

Radar assimilation

The assimilation of radar reflectivity and radial velocity improves model predictions of the location and structure of MCS and reduces the convection intensity. Statistical metrics indicate that reflectivity RMSE is substantially reduced from the beginning of radar assimilation to the end of radar assimilation, and its consistency ratio remains stable around 1. Meanwhile, the assimilation of radar reflectivity and radial velocity also corrects the water vapor vertical profile, when compared with the ALVICE lidar observed water vapor mixing ratio. After assimilating radar data, the WRF model more accurately forecasts the generation of bore waves.

After successfully assimilating radar data into the WRF model, the next steps will be to debug the ALVICE lidar assimilation and improve the model simulation results. After assimilating ALVICE lidar successfully, the other three lidars will be assimilated. All designed experiments shown in Table 2 will be conducted.

References

He, J., Zhang, F., Chen, X., Bao, X., Chen, D., Kim, H. M., ... & Yang, K. (2019). Development and evaluation of an ensemble-based data assimilation system for regional reanalysis over the Tibetan Plateau and surrounding regions. Journal of Advances in Modeling Earth Systems, 11(8), 2503-2522. https://doi.org/10.1029/2019MS001665.

Iacono, M., J. S. Delamere, E. J. Mlawer, M. W. Shephard, S. A. Clough, and W. D. Collins, 2008: Radiative forcing by long-lived greenhouse gases: Calculations with the AER radiative transfer models. J. Geophys. Res., 113, D13103, https://doi.org/10.1029/2008JD009944.

Janjić, Z. I., 1994: The step-mountain eta coordinate model: Further developments of the convection, viscous sublayer, and turbulence closure schemes. Mon. Wea. Rev., 122, 927–945, https://doi.org/10.1175/1520-0493(1994)122<0927:TSMECM>2.0.CO;2.

Janjić, Z. I., 1996: The surface layer in the NCEP Eta Model. Preprints, 11th Conf. on Numerical Weather Prediction, Norfolk, VA, Amer. Meteor. Soc., 354–355.

Ek, M. B., K. E. Mitchell, Y. Lin, E. Rogers, P. Grunmann, V. Koren, G. Gayno, and J. D. Tarpley, 2003: Implementation of Noah land surface model advances in the National Centers for Environmental Prediction operational mesoscale Eta model. J. Geophys. Res., 108, 8851, https://doi.org/10.1029/2002JD003296.

Thompson, G., P. R. Field, R. M. Rasmussen, and W. D. Hall, 2008: Explicit forecasts of winter precipitation using an improved bulk microphysics scheme. Part II: Implementation of a new snow parameterization. Mon. Wea. Rev., 136, 5095–5115, https://doi.org/10.1175/2008MWR2387.1.

Weckwerth, T. M., J. Hanesiak, J. W. Wilson, S. B. Trier, S. K. Degelia, W. A. Gallus, ... & X. Wang, 2019: Nocturnal convection initiation during PECAN 2015. Bulletin of the American Meteorological Society, 100(11), 2223-2239, https://doi.org/10.1175/BAMS-D-18-0299.1.

Weng, Y., and F. Zhang, 2012: Assimilating airborne Doppler radar observations with and ensemble Kalman filter for convection- permitting hurricane initialization and prediction: Katrina (2005). Mon. Wea. Rev., 140, 841–859, https://doi.org/10.1175/ 2011MWR3602.1.

Zhang, F., Y. Weng, J. A. Sippel, Z. Meng, and C. H. Bishop, 2009: Cloud-resolving hurricane initialization and prediction through assimilation of Doppler radar observations with an ensemble Kalman filter. Mon. Wea. Rev., 137, 2105–2125, https://doi.org/ 10.1175/2009MWR2645.1.

Zhang, Y., D. J. Stensrud, and F. Zhang, 2019: Simultaneous assimilation of radar and all-sky satellite infrared radiance observations for convection-allowing ensemble analysis and prediction of severe thunderstorms. Monthly Weather Review, 147(12), 4389-4409, https://doi.org/10.1175/MWR-D-19-0163.1.